

Pollen-based reconstructions of Holocene climate trends in the eastern Mediterranean region

Esmeralda Cruz-Silva^{1,*}, Sandy P. Harrison¹, I. Colin Prentice², Elena Marinova³, Patrick J. Bartlein⁴, Hans Renssen⁵, Yurui Zhang⁶

1: School of Archaeology, Geography & Environmental Science, Reading University, Whiteknights, Reading, RG6 6AH, UK

2: Georgina Mace Centre for the Living Planet, Department of Life Sciences, Imperial College London, Silwood Park Campus, Buckhurst Road, Ascot SL5 7PY, UK

3: Laboratory for Archaeobotany, Baden-Württemberg State Office for Cultural Heritage Management, Fischersteig 9, 78343 Hemmenhofen-Gaienhofen, Germany

4: Department of Geography, University of Oregon, Eugene, Oregon 97403-1251 USA

5: Department of Natural Sciences and Environmental Health, University of South-Eastern Norway, Bø, Norway

6: State Key Laboratory of Marine Environmental Science, College of Ocean & Earth Sciences, Xiamen University, Xiamen, China

*: Corresponding author

Ms for Climate of the Past

1 Abstract

2 There has been considerable debate about the degree to which climate has driven societal changes in the
3 eastern Mediterranean region, partly through reliance on a limited number of qualitative records of climate
4 changes and partly reflecting the need to disentangle the joint impact of changes in different aspects of
5 climate. Here, we use tolerance-weighted Weighted Averaging Partial Least Squares to derive reconstructions
6 of mean temperature of the coldest month (MTCO), mean temperature of the warmest month (MTWA),
7 growing degree days above a threshold of 0°C (GDD0) and plant-available moisture, represented by the ratio
8 of modelled actual to equilibrium evapotranspiration (α) and corrected for past CO₂ changes for 71 individual
9 pollen records from the Eastern Mediterranean region covering part or all of the interval from 12.3 ka to the
10 present. We use these reconstructions to create regional composites that illustrate the long-term trends in
11 each variable. We compare these composites with transient climate model simulations to explore potential
12 causes of the observed trends. We show that the glacial-Holocene transition and the early part of the Holocene
13 was characterised by conditions colder than present. Rapid increases in temperature occurred between ca
14 10.3 and 9.3 ka, considerably after the end of the Younger Dryas. Although the time series are characterised
15 by centennial-to-millennial oscillations, MTCO showed a gradual increase from 9 ka to the present, consistent
16 with the expectation that winter temperatures were forced by orbitally-induced increases in insolation during
17 the Holocene. MTWA also showed an increasing trend from 9 ka and reached a maximum of ca 1.5°C greater
18 than present at ca 4.5 and 5 ka, followed by a gradual decline towards present-day conditions. A delayed
19 response to summer insolation changes is likely a reflection of the persistence of the Laurentide and
20 Fennoscandian ice sheets; subsequent summer cooling is consistent with the expected response to insolation
21 changes. Plant-available moisture increased rapidly after 11 ka and conditions were wetter than today
22 between 10-6 ka, but thereafter α declined gradually. These trends likely reflect changes in atmospheric
23 circulation and moisture advection into the region, and were probably too small to influence summer
24 temperature through land-surface feedbacks. Differences in the simulated trajectory of α in different models
25 highlight the difficulties in reproducing circulation-driven moisture advection into the eastern Mediterranean.

1. Introduction

27 The Eastern Mediterranean region is a critical region for examining the long-term interactions between climate
28 and past societies because of the early adoption of agriculture in the region, which has been widely associated
29 with the rapid warming at the end of the Younger Dryas (Belfer-Cohen and Goring-Morris, 2011). Societal
30 collapse and large-scale migrations have been associated with climates less favourable to agriculture during
31 the 8.2 ka event (Weninger et al., 2006) or to major changes in agricultural practices (Roffet-Salque et al.,
32 2018). Subsequent periods of less favourable climate, particularly prolonged droughts, have been associated
33 with the fall of the Akkadian empire ca. 4.2 ka (Cookson et al., 2019), and the end of the Late Bronze Age and
34 the beginning of the Greek Dark Ages ca 3.2 ka (Kaniewski et al., 2013; Drake, 2012). However, the attribution
35 of changes in human society to climate changes is not universally accepted. Flohr et al. (2016), for example,
36 analysed radiocarbon-dated archaeological sites for evidence of societal changes in response to climate
37 changes in the early Holocene, particularly the 8.2 ka event, and found no evidence of large-scale site
38 abandonment or migration although there were indications of local adaptations. However, since Flohr et al.
39 (2016) did not compare the archaeological records to region-specific climate reconstructions, it is difficult to
40 assess how far local responses might reflect differences in climate between the sites. Even the societal
41 response to the early Holocene warming appears to have differed across the region (Roberts et al., 2018).

42 The need to understand the interactions between climate and past societies in the Eastern Mediterranean is
43 given further impetus because human modification of the landscape has the potential to affect climate directly
44 through changes in land-surface properties. The degree to which human modifications of the landscape had a
45 significant impact on global climate before the pre-industrial period is debated (Ruddiman, 2003; Joos et al.,
46 2004; Kaplan et al., 2011; Singarayer et al., 2011; Mitchell et al., 2013; Stocker et al., 2017), but these impacts
47 were likely to be more important in regions with a long history of settlement and agricultural activities
48 (Harrison et al., 2020).

49 Much of our current understanding of climate changes in the Eastern Mediterranean region is based on the
50 qualitative interpretation of individual records (e.g. Roberts et al., 2019). Oxygen-isotope records from
51 speleothems or lake sediments have been used to infer changes in moisture availability through the Holocene
52 (e.g. Bar-Matthews et al., 1997; Cheng et al., 2015; Dean et al., 2015; Burstyn et al., 2019) as have pollen-
53 based reconstructions of changes in vegetation (e.g. Bottema, 1995; Denèfle et al., 2000; Sadori et al., 2011).
54 Pollen records can also be used to make quantitative reconstructions of seasonal temperatures, and
55 precipitation or plant-available water (Bartlein et al., 2011; Chevalier et al., 2020). Quantitative
56 reconstructions of past climates have been made for individual records from the Eastern Mediterranean
57 region (e.g. Cheddadi and Khater, 2016; Magyari et al., 2019), and syntheses of pollen-based quantitative
58 climate reconstructions have included sites from this region (Davis et al., 2003; Mauri et al., 2015; Herzschuh
59 et al., 2022). Davis et al. (2003) provided a composite curve of seasonal temperature changes, but not moisture
60 changes; both summer and winter temperatures showed very little variation ($<1^{\circ}\text{C}$) through most of the
61 Holocene. Mauri et al. (2015) is an updated version of the Davis et al. (2003) reconstructions, with more sites
62 included but showing similarly muted temperate changes in the Eastern Mediterranean region. Herzschuh et
63 al. (2022) showed more homogenous changes in both temperature and precipitation across the Eastern
64 Mediterranean region but it is difficult to compare the two reconstructions directly because they used
65 different reconstruction techniques. None of the existing reconstructions take account of the impact of
66 changing CO_2 levels on vegetation which could potentially affect the reconstructions of moisture variables
67 (Prentice et al., 2022). Thus, there is a need for well-founded reconstructions of climate, particularly climate

68 variables that are relevant for human occupation and agriculture, to be able to address questions about the
69 interactions between climate and society in the Eastern Mediterranean region.

70 Here, we provide new quantitative reconstructions of seasonal temperature and plant-available moisture for
71 71 sites from the Eastern Mediterranean region (defined by the Eastern Mediterranean-Black Sea-Caspian
72 Corridor, EMBSecBIO, project as the region between 20°E – 62°E, 29°N – 49°N), including a correction for the
73 impact of changing CO₂ levels on plant-available moisture reconstructions. We use these reconstructions to
74 document the regional trends in climate from 12.3 ka to the present. We then explore how far these trends
75 can be explained by changes in external forcing by comparing the reconstructions with transient climate model
76 simulations.

77

78 **2. Methods**

79 **2.1. Modern pollen and climate data**

80 The modern pollen dataset was obtained from version 1 of the SPECIAL Modern Pollen Data Set (SMPDSv1,
81 Harrison, 2019), which provides relative abundance data from 6459 terrestrial sites from Europe, the Middle
82 East and northern Eurasia, assembled from multiple public sources or provided by the original authors. The
83 SMPDS pollen records have been taxonomically standardized, filtered to remove obligate aquatics,
84 insectivorous species, introduced species, or taxa that only occur in cultivation, and to group taxa with only
85 sporadic occurrences into higher taxonomic levels (genus, sub-family or family) and consequently provides
86 relative abundance data for 247 pollen taxa (Supplementary Table 1). We used the 5840 SMPDS sites from the
87 area between 20°W to 62°E and 29°N and 75°N to construct the training data set (Supplementary Figure 1);
88 the sampling outside this box is limited and likely not representative of the diversity of the climate gradients.
89 At sites with multiple modern samples, we averaged the taxon abundances across all samples, to minimise
90 over-representation of some localities and hence specific climates, in the training dataset. We used the 195
91 pollen taxa that occurred at more than 10 sites (Supplementary Table 1) to derive climate-abundance
92 relationships.

93 We focus on reconstructing bioclimatic variables that fundamentally control plant distribution, specifically
94 related to winter temperature limits, accumulated summer warmth and plant-available moisture (Harrison et
95 al., 2010). The bioclimatic data for each modern site was obtained from Harrison et al. (2019), a dataset that
96 provides estimates of mean temperature of the coldest month (MTCO), growing degree days above a base
97 level of 0°C (GDD0), and a moisture index (MI) defined as the ratio of annual precipitation to annual potential
98 evapotranspiration at each modern pollen site, derived using a geographically-weighted regression of version
99 2.0 of the Climate Research Unit (CRU) long-term gridded climatology at 10 arc minute resolution (CRU CL
100 v2.0; New et al., 2002). MTCO and GDD0 were taken directly from the data set. Since Harrison et al. (2019) do
101 not provide mean temperature of the warmest month (MTWA), we calculated this based on the relationship
102 between MTCO and GDD0 given in Wei et al. (2021). We derived an alternative moisture index, α , which is the
103 ratio between modelled actual and equilibrium evapotranspiration, from MI following Liu et al. (2020). MI and
104 α both provide good indices of plant-available moisture, but since α has a natural limit in wetter conditions it
105 is more suitable for discriminating differences in drier climates.

106 2.2. Fossil pollen data

107 The fossil pollen dataset for eastern Mediterranean region was obtained from the Eastern Mediterranean-
108 Black Sea Caspian Corridor (EMBSecBIO) database (Harrison et al., 2021), which contains information from
109 187 records from the region between 20°E and 62°E and between 29°N and 49°N. (Note this is a more limited
110 region than used for the modern training data set.) We discarded records (a) from marine environments or
111 very large lakes (>500 km²), (b) with no radiocarbon dating, (c) where the age of the youngest pollen sample
112 was unknown, (d) where there is an hiatus after the youngest radiocarbon date, (e) where more than half of
113 the radiocarbon dates were rejected by the original authors, and (f) where more than half of the ages were
114 based on pollen correlation with other radiocarbon-dated records. However, we kept records where there is
115 an hiatus but where there are sufficient radiocarbon dates above the hiatus to create an age model for the
116 post-hiatus part of the record. We constructed new age models for all the remaining sites (121) using the
117 IntCal20 calibration curve (Reimer et al., 2020) and the 'rbacon' R package (Blaauw et al., 2021) in the
118 framework of the 'AgeR' R package (Villegas-Diaz et al., 2021). Some of these records have no modern samples,
119 where modern was defined as 0-300 yr BP, and thus could not be used to calculate climate anomalies. As a
120 result, 71 pollen records (Figure 1; Supplementary Table 2) were used for the climate reconstructions. These
121 records have a mean length of 6594 years and a mean resolution of 228 years. The records were taxonomically
122 standardized for consistency with the training dataset.

123 2.3 Climate reconstructions

124 We used tolerance-weighted Weighted Averaging Partial Least Squares (*fxTWA-PLS*, Liu et al., 2020) regression
125 to model the relationships between taxon abundances and individual climate variables in the modern training
126 dataset and then applied these relationships to reconstruct past climate using the fossil assemblages. *fxTWA-*
127 *PLS* reduces the known tendency of regression methods to compress climate reconstructions towards the
128 middle of the sampled range by applying a sampling frequency correction to reduce the influence of uneven
129 sampling of climate space, and by weighting the contribution of individual taxa according to their climate
130 tolerance (Liu et al., 2020). Version 2 of *fxTWA-PLS* (*fxTWA-PLS2*, Liu et al., 2023), applied here, uses P-spline
131 smoothing to derive the frequency correction and also applies the correction both in estimating climate
132 optima and in the regression itself, producing a further improvement in model performance relative to version
133 1 as published by Liu et al. (2020).

134 We evaluated the *fxTWA-PLS* models by comparing the reconstructions against observations using pseudo-
135 removed leave-out cross-validation, where one site was randomly selected as a test site and geographically
136 and climatically similar sites (pseudo sites) were removed from the training set to avoid redundancy in the
137 climate information inflating the cross-validation. We selected the last significant component (p -value ≤ 0.01)
138 and assessed model performance using the root mean square error of prediction (RMSEP). The degree of
139 compression was assessed using linear regression and local compression was assessed by loess regression
140 (*locfit*). Climate reconstructions were made for every sample in each fossil record using the best models and
141 sample specific errors were estimated via bootstrapping. We applied a correction factor (Prentice et al., 2022)
142 to the reconstructions of α to account for the impact of changes in atmospheric CO₂ levels on water-use
143 efficiency, specifically the increased water use efficiency under high CO₂ levels characteristic of the recent past
144 and the low CO₂ levels that would have reduced water use efficiency during the late glacial and thus could
145 have influenced the reconstructions during the earliest part of the records. The correction was implemented
146 through the package *codos*: 0.0.2 (Prentice et al., 2022) with past CO₂ concentration values derived from the
147 EPICA Dome C record (Bereiter et al., 2015).

148 **2.4. Construction of climate time series**

149 To obtain climate time series representative of the regional trends in climate, we first screened the
150 reconstructions to remove individual samples with (a) low effective diversity (< 2) as measured using Hill's N_2
151 diversity measure (Hill, 1973), which could indicate low pollen counts or local contamination, and (b) sample-
152 specific errors above the 0.95 quantile to remove obvious outliers. This screening resulted in the exclusion of
153 only a small number of individual samples (see Supplementary Figure 2). We then averaged the reconstructed
154 values in 300-year bins (slightly larger than the average resolution of the records, 228 years) with 50% overlap.
155 The first bin centred on 150 yr BP, and subsequent bins were centred at 150 yr increments throughout the
156 record. We excluded any bins with only one sample. The binned values of individual sites were averaged to
157 produce a regional composite of the anomalies for each climate variable, where the modern baseline was
158 taken as the first 300-yr bin centred on 150 yr BP. These time series were smoothed using locally weighted
159 regression (Cleveland & Devlin, 1988) with a window width of 1000 years (half-window width 500 years) and
160 fixed target points in time to highlight the long-term trends. Confidence intervals (5th and 95th percentiles) for
161 each composite were generated by bootstrap resampling by site over 1000 iterations. We examined the
162 impact of the CO₂ correction on reconstructed α (Supplementary Figure 3); this had no major effect on the
163 reconstructed trends except during the earliest part of the record.

164 **2.5. Climate model simulations**

165 We compared the reconstructed climate changes with transient climate model simulations of the response to
166 external forcing, to determine the extent that the reconstructed climate changes reflect changes in known
167 forcing. We used transient simulations of the response to orbital and greenhouse gas forcing in the later
168 Holocene from four models participating in the PAleao-Constraints on Monsoon Evolution and Dynamics
169 (PACMEDY) project (Carré et al., 2021): the MPI (Max Planck Institute) Earth System Model version 1.2
170 (Dallmeyer et al., 2020), the AWI (Alfred Wegener Institute) Earth System Model version 2 (Sidorenko et al.,
171 2019), and two versions of the IPSL (Institut Pierre Simon Laplace) Earth System Model. The IPSL and AWI
172 simulations were run from 6 ka to 1950 CE, the MPI simulation from 7.95 ka to 1850 CE. We used a longer
173 transient simulation covering the period from 11.5 ka made with the LOVECLIM model (Goosse et al., 2010)
174 which, in addition to orbital and greenhouse gas forcing, accounts for the waning of the Laurentide and
175 Fennoscandian ice sheets (Zhang et al., 2016). Finally, we used two transient simulations from 22 ka to present
176 made using the Community Climate System Model (CCSM3; Collins et al., 2006). Both were forced by changes
177 in orbital configuration, atmospheric greenhouse gas concentrations, continental ice sheets and meltwater
178 fluxes, but differ in the configuration of the meltwater forcing applied after the Bølling warming (14.7 ka). In
179 the first simulation (TRACE-21k-I: Liu et al., 2009), there was a sustained meltwater flux of ~ 0.1 Sv from the
180 Northern Hemisphere ice sheets to the Arctic and North Atlantic until ca 6 ka, and a continuous inflow of water
181 from the North Pacific into the Arctic after the opening of the Bering Strait. The second simulation (TRACE-
182 21k-II; He and Clark, 2022) had no meltwater flux during the Bølling warming or the Holocene but applied a
183 flux of ~ 0.17 Sv to the North Atlantic during the Younger Dryas (12.9-11.7 ka). The difference in meltwater
184 forcing results in a much stronger Atlantic Meridional Overturning Circulation during the Holocene in the
185 TRACE-21k-II simulation compared to the TRACE-21k-I simulation. Details of the model simulations are given
186 in Supplementary Table 3. The use of multiple simulations allows the identification of robust signals that are
187 not model-dependent (see e.g. Carré et al., 2021) and also the separation of the effects of different forcings.
188 The TraCE-21k-I data were adjusted to reflect the changing length of months during the Holocene, (related to
189 the eccentricity of Earth's orbit and the precession-determined time of year of perihelion), whereas the other

190 simulations were not. However, this makes little practical difference for the selection of variables used here
191 (Supplementary Figure 4).

192 Outputs from each simulation were extracted for land grid cells in the EMBSecBIO domain (20° E – 55° E, 29° N
193 – 49° N; this region extends slightly less far eastwards than the EMBSecBIO region as originally defined but
194 there are no pollen sites beyond 55° E). MTCO and MTWA were extracted directly; GDD0 was obtained by
195 deriving daily temperature values from monthly data using a mean-preserving autoregressive interpolation
196 function (Rymes & Myers, 2001). Daily values of cloud cover fraction and precipitation were obtained from
197 monthly data in the same way, and used to estimate MI, i.e. the ratio of annual precipitation to annual
198 potential evapotranspiration, through the R package *smpds* (Villegas-Diaz & Harrison, 2022) before converting
199 this to α following Liu et al. (2020). For consistency with the reconstructed time series, climate anomalies for
200 30-yr bins for each land grid cell within the EMBSecBIO domain were calculated using the interval after 300 yr
201 BP as the modern baseline. Since the spatial resolution of the models varies (Supplementary Table 3), and in
202 any case is coarser than the sampling resolution of the individual pollen records precluding direct comparisons
203 except at a regional scale, we used all of the land grid cells within the EMBSecBIO domain and did not attempt
204 to select grid cells coincident with the location of pollen data. A composite was produced by averaging the
205 grid cell time series, which was then smoothed using locally weighted regression (Cleveland & Devlin, 1988)
206 with a window width of 1000 years (i.e. a half-window width of 500 years) and fixed target points in time.
207 Confidence intervals (5th and 95th percentiles) for each composite were generated by bootstrap resampling
208 by grid cell over 1000 iterations.

209 **3. Results**

210 **3.1. Performance of the fxTWA-PLS statistical model**

211 The assessment of the model through cross-validation showed that it reproduces the modern climate variables
212 reasonably well (Table 1, Supplementary Table 4). The best performance is achieved by α ($R^2 = 0.73$, RMSEP =
213 0.15) and MTCO ($R^2 = 0.73$, RMSEP 3.7°). The models for GDD0 ($R^2 = 0.69$, RMSEP = 880) and MTWA ($R^2 = 0.63$,
214 RMSEP = 3.22) were also acceptable. The slopes of the regressions ranged from 0.78 (MTWA) to 0.86 (MTCO),
215 indicating that the degree of compression in the reconstructions is small (Table 1). Thus, the downcore fxTWA-
216 PLS reconstructions of all the climate variables can be considered to be robust and reliable.

217 **3.2. Holocene climate evolution in the region**

218 Down-core reconstructions showed broadly coherent signals, although there was variation in both the timing
219 and magnitude of climate changes across the sites, reflecting differences in latitude and elevation (Figures 2,
220 3, 4). Nevertheless, the records indicated coherent regional trends over the past 12 ky.

221 Winter temperature showed a cooling trend between 12 and 11 ka, with reconstructed MTCO ca 8°C lower
222 than present at 11 ka (Figure 5). There was a moderate increase in MTCO after 11 ka, followed by a more
223 pronounced increase of ca 5°C between 10.3 and 9.3 ka. Winter temperatures were only ca 2°C lower than
224 present at the end of this rapid warming phase. There are relatively large uncertainties on the MTCO
225 reconstructions prior to 10.3 ka, so the trends in the early part of the record are not well constrained. However,
226 the phase of rapid warming between 10.3 and 9.3 ka (and the subsequent part of the record) is well
227 constrained. MTCO continued to increase gradually through the Holocene, although multi-centennial to
228 millennial oscillations were superimposed on the general trend.

229 The initial trends in summer temperature were broadly similar to those in MTCO, with a cooling between 12.3
230 and 11ka and reconstructed MTWA ca 2°C lower than present at 11 ka (Figure 5). Summer temperature

231 increased thereafter, albeit with pronounced millennial oscillations, up to ca 4.5 ka when MTWA was ca 1.5°C
232 higher than present. There was a gradual decrease in summer temperature after ca 4.5 ka. The GDDO
233 reconstructions showed similar trends to MTWA, reaching maximum values around 4.5 ka when the growing
234 season was ca 150 degree days greater than today. The subsequent decline in GDDO was somewhat flatter,
235 which presumably reflects the influence of still-increasing winter temperatures on the length of the growing
236 season.

237 The trends in α differ from the trends in temperature. Conditions were similar to present around 11.5 ka
238 (Figure 5). Between 11 and 10 ka, there was a rapid increase in α . Values of α were higher than present (>0.1)
239 between 10 to 6 ka. Subsequently, there was a gradual and continuous decrease in α until the present time.
240 The correction for the physiological impact of CO₂ levels was, as expected, largest during intervals when CO₂
241 was lowest (i.e. prior to 11 ka) (Supplementary Figure 4). The reconstructions with and without the correction
242 are not statistically different between 10 and 5 ka, taking account the uncertainties in the reconstructions, but
243 the correction produced marginally wetter reconstructions after 5 ka, with a maximum difference of 0.08.
244 However, the gradually declining trend in moisture availability towards the present is not affected by the CO₂
245 correction.

246 **3.3. Comparison with climate simulations**

247 The TRACE-21k-I simulation (Figure 6) shows an initial winter warming between 12-11 ka but MTCO is still ca
248 3°C lower than present at 11 ka. There is a gradual increase in MTCO from 11 ka onwards, although with
249 centennial-scale variability and a more pronounced oscillation corresponding to the 8.2 ka event. The TRACE-
250 21k-II simulation is initially slightly colder and displays a two-step warming with a peak at 8.5 ka, when MTCO
251 is ca 1.5°C lower than present. The later Holocene trend is similar to that shown in TRACE-21k-I. The LOVECLIM
252 simulation produced generally warmer conditions than either of the TRACE simulations: MTCO is ca 2.5°C
253 lower than present at 11 ka but the two-step warming is more pronounced and peak warming occurs
254 somewhat later at ca 7.5 ka when MTCO was only ca 0.25°C lower than present (Figure 7). While all three
255 models show a rapid warming comparable to the reconstructed warming between 10.3 and 9.3 ka, it is clear
256 that differences in the ice sheet and meltwater forcings affect both the magnitude and the timing of this trend.
257 The overall magnitude of the warming after 9 ka in the TRACE-21k-I simulation is consistent with the
258 reconstructions of MTCO (anomalies of 2.4°C and 2.6°C for model and data respectively). The mid-to late
259 Holocene trend is similar in the PACMEDY simulations (Figure 8) to both TRACE-21k simulations, both in sign
260 and in magnitude (ca 1°C between 6 ka and present) and both are consistent with the reconstructions ($-0.9 \pm$
261 0.7°C). The continuous increase of MTCO is consistent with the change in winter insolation. Given the
262 similarities between the PACMEDY simulations (which only include orbital and greenhouse gas forcing) and
263 the LOVECLIM and TRACE simulations, which also include forcing associated with the relict Laurentide and
264 Fennoscandian ice sheets, it seems likely that orbital forcing was the main driver of winter temperatures in
265 the EMBSecBIO region during the later Holocene.

266 The TRACE-21k-I simulation shows peak summer temperatures between 11-9 ka, when MTWA was ca. 3°C
267 greater than present (Figure 6). The TRACE-21K-II simulations is initially colder than the TRACE-21k-I
268 simulation and the peak in summer temperatures occurs at 9 ka, when MTWA was ca 2.5°C greater than
269 present (Figure 6). The LOVECLIM simulation is warmer than present from 11.5 ka, but peak warming is only
270 reached at 7.5 ka when MTWA is ca 2°C (Figure 7). All three simulations show a gradual decrease in summer
271 temperature through the Holocene after this initial peak. This decreasing trend is also seen in the PACMEDY
272 simulations from 6 ka (or 8 ka in the case of the MPI simulation) onwards (Figure 8) and the magnitude of the
273 change over this interval (ca 2°C from 6ka onwards) is similar to that shown by the TRACE and the LOVECLIM

274 simulations. This similarity suggests that the simulated response is a direct reflection of the change in orbital
275 forcing. However, the reconstructed changes in summer temperature do not show this gradual decline.
276 Reconstructed MTWA is ca 4°C colder than the model predictions at 9 ka. The reconstructions show a gradual
277 increase in MTWA from 9 to 4.5 ka. Changes in reconstructed temperatures at 4.5 ka are of a similar magnitude
278 to simulated temperatures at this time (ca 1°C greater than present) although the late Holocene is marked by
279 a cooling trend as seen in the simulations. Thus, while the simulated late Holocene trend is consistent with
280 orbital forcing being the main driver of summer temperatures in the EMBSecBIO region, the early to mid-
281 Holocene trend is not. Previous modelling studies have suggested that the timing of peak warmth differs in
282 different regions of Europe and is associated with the impact of the Fennoscandian ice sheet on regional
283 climates (Renssen et al., 2009; Blascheck and Renssen, 2013; Zhang et al., 2016). The differences in the timing
284 of peak warmth in the EMBSecBIO region in the TRACE-21k-II and LOVECLIM simulations would be consistent
285 with this argument but suggest that the timing and magnitude are model-dependent. It is therefore plausible
286 that the reconstructed trend in MTWA at least during the early Holocene reflects the influence of the relict
287 Laurentide and Fennoscandian ice sheets in modulating the impact of increased summer insolation until the
288 mid-Holocene. Given that GDD0 is a reflection of both changes in season length, as influenced by winter
289 temperatures, and summer warming, the difference between simulated and reconstructed MTWA are also
290 seen in GDD0 trends during the early part of the Holocene (Figure 6).

291 The simulations do not show consistent patterns for the trend in α . The TRACE-21k-I simulation (Figure 6)
292 shows a gradual increase, with minor multi-centennial oscillations from 12 ka to present. (Available model
293 output variables are not sufficient to calculate α for the TRACE-21k-II or LOVECLIM simulations). One of the
294 PACMEDY simulations (IPSL-CM5) shows an increase from the mid-Holocene (Figure 8) although the simulated
295 change is an order of magnitude smaller than over the comparable period in the TRACE-21k-I simulation. The
296 AWI model shows no trend in α over this period; the remaining two models show increasing aridity from the
297 mid-Holocene to present (Figure 8). These three models are all broadly consistent with the reconstructions
298 since the reconstructed decrease in α is small. However, the differences in the sign of the trend between the
299 different models indicates that changes in moisture are not a straightforward consequence of the forcing, but
300 must reflect model-dependent changes in moisture supply via changes in atmospheric circulation.
301 Reconstructions of Holocene climates in Iberia have suggested that land-surface feedbacks associated with
302 changes in moisture availability have a strong influence on summer temperature (Liu et al., 2023). There does
303 not seem to be strong evidence for this in the EMBSecBIO region, given the difference in the trends of α and
304 MTWA and the muted nature of the trend in α .

305

306 **4. Discussion**

307 The three temperature-related variables, MTCO, MTWA and GDD0 all show relatively warm conditions around
308 the late glacial/Holocene transition (ca 12 ka) followed by a cooling that was greatest between ca 11 and 10
309 ka. This pattern is also shown in regional composites (Figure 9) derived from the reconstructions by Mauri et al.
310 al. (2015) and Herzschuh et al. (2022). However, the magnitude of the cooling shown in the Mauri et al. (2015)
311 and Herzschuh et al. (2022) reconstructions is small compared to our reconstructions. The cool interval starts
312 somewhat later and persists until 9 ka in the Mauri et al. (2015) reconstructions, but this is partly a reflection
313 of the fact that these reconstructions were only made at 1 ka intervals and thus the transitions are less well
314 constrained than in either our reconstructions or those of Herzschuh et al. (2022). This cool interval and the
315 marked warming seen after 10.3 ka in our reconstructions, does not correspond to the Younger Dryas and the

316 subsequent warming. Although the Younger Dryas is considered to be a globally synchronous event (Cheng et
317 al., 2020) and is generally considered coeval with Greenland Stadial I (Larsson et al., 2022), it does not appear
318 to be strongly registered in the EMBSeCBIO region in any of the quantitative climate reconstructions. This is
319 consistent with earlier suggestions based on vegetation changes that the Younger Dryas was not a clearly
320 marked feature over much of this region (Bottema, 1995).

321 We have shown that winter temperatures increased sharply between 10.3 and 9.3 ka, but then continued to
322 increase at a more gradual rate through the Holocene. The increase of ca 7.5°C is of the same order of
323 magnitude to the increase shown in the TRACE-21K-II simulation (ca. 5°C) and in the LOVECLIM simulation (ca.
324 3°C). This increasing trend is also seen in the Mauri et al. (2015) reconstructions of MTCO (Figure 9), although
325 the change from the early Holocene to the present is much smaller (ca 0.5–1°C) in these reconstructions than
326 in our reconstructions and Mauri et al. (2015) do not show marked cooling around 11 ka. Nevertheless, the
327 consistency between the two reconstructions and between our reconstruction and the simulated changes in
328 MTCO supports the idea that these trends are a response to orbital forcing during the Holocene. Our
329 reconstructions show a gradual increase in summer temperature, as measured by both MTWA and GDD0,
330 from ca 10 to 5 ka when MTWA was ca 1°C warmer than present, followed by a gradual decrease towards the
331 present. This is not consistent with previous reconstructions. Mauri et al. (2015) show an overall increasing
332 trend from 9 ka to present. The Herzschuh et al. (2022) shows a completely different pattern, with the
333 maximum in July temperature at ca. 9 ka and an oscillating but declining trend thereafter (Figure 9).

334 These differences between the three sets of reconstructions are too large to be caused by differences in the
335 age models applied. They are also unlikely to reflect differences in sampling, since the number of sites used is
336 roughly similar across all three reconstructions (71 sites versus 67 sites from Herzschuh et al., 2022 and 409
337 grid points, based on 57 sites, from Mauri et al., 2015); most sites are common to all three analyses. The
338 differences must therefore be related to the reconstruction method. Herzschuh et al. (2022) used the
339 regression-based approach, Weighted Average Partial Least Squares (WA-PLS), that is the basis for our
340 reconstruction technique, fxTWA-PLSv2. Mauri et al. (2015) used the modern analogue technique. However,
341 after taking account of differences caused by the temporal resolution, there is greater similarity between our
342 reconstructions and those of Mauri et al. (2015) than between either of these reconstructions and the
343 Herzschuh et al. (2022) reconstructions.

344 Several methodological issues could be responsible for the differences between the three sets of
345 reconstructions, and in particular the anomalous moisture trends shown by Herzschuh et al. (2022).
346 Specifically, Herzschuh et al. (2022) used (1) a unique calibration data set for each fossil site based on modern
347 samples within a 2000 km radius of that site, rather than relying on a single training data set; (2) a limited set
348 of 70 dominant taxa rather than the whole pollen assemblage; and (3) included marine records from e.g. the
349 Black Sea, which were excluded in the other reconstructions because they sample an extremely large area and
350 thus are unrepresentative of the local climate.

351 Reconstructed MTWA shows a gradual increase through the early Holocene with maximum values of around
352 1.5°C greater than present reached at ca 4.5 ka. Previous modelling studies have shown the timing of
353 maximum warmth during the Holocene in Europe was delayed compared to the maximum of insolation forcing
354 and varied regionally as a consequence of the impact of the Fennoscandian ice sheet on surface albedo,
355 atmospheric circulation and heat transport (Renssen et al., 2009; Blascheck and Renssen, 2013; Zhang et al.,
356 2016; Zhang et al., 2023). Two of the simulations examined here show a delay in the timing of peak warmth,
357 which occurred ca 9 ka in the TRACE-21k-II simulation and ca 7.5 ka in the LOVECLIM simulation. Although
358 both sets of simulations include the relict Laurentide and Fennoscandian ice sheets, neither has realistic ice

359 sheet and meltwater forcing. In the LOVECLIM simulation, for example, the Fennoscandian ice sheet was gone
360 by 10 ka whereas in reality it persisted until at least 8.7 ka (Patton et al., 2017). Thus, the impact of the
361 Fennoscandian ice sheet in delaying orbitally induced warming would likely have been greater than shown in
362 this simulation. In addition to differences in the way in which ice sheets and meltwater forcing are
363 implemented in different models, models are also differentially sensitive to the presence of the same
364 prescribed ice sheet (Kapsch et al., 2022). Thus, it would be useful to examine the influence of more realistic
365 prescriptions of the relict ice sheets on the climate of the EMBSecBIO region using multiple models, and
366 preferably transient simulations at higher resolution or regional climate models. It has been suggested that
367 meltwater was routed to the Black and Caspian Seas via the Dnieper and Volga Rivers during the early phase
368 of deglaciation (e.g. Yanchilina et al., 2019; Aksu et al. 2022; Vadsaria et al., 2022) and it would also be useful
369 to investigate the impact of this on the regional climate.

370 We have shown that α was similar to today around 11 ka, but there was a rapid increase in moisture availability
371 after ca 10.5 ka such that α values were noticeably higher than present between 10 to 6 ka, followed by a
372 gradual and continuous decrease until the present time. Changes in the late Holocene are small even at
373 centennial scale (Figure 5). The reconstructed trends in α are not captured in the simulations, which show
374 different trends during the late Holocene. Thus, it is unlikely that the gradual increase in aridity during the late
375 Holocene is a straight-forward response to orbital forcing. Changes in α in the EMBSecBIO region are likely to
376 be primarily driven by precipitation changes, which in turn are driven by changes in atmospheric circulation.
377 Differences in the trend of moisture availability between the models imply that the nature of the changes in
378 circulation varies between models and thus the simulations do not provide a strong basis for explaining the
379 observed patterns of change in moisture availability. Earlier studies, focusing on the western Mediterranean
380 (Liu et al., 2023), Europe (Mauri et al., 2014) and central Eurasia (Bartlein et al., 2017), have shown that models
381 have difficulty in simulating the enhanced moisture transport into the Eurasian continent shown by
382 palaeoenvironmental data during the mid-Holocene and during the late Holocene. Changes in precipitation
383 can also affect land-surface feedbacks. Liu et al. (2023), for example, have argued that enhanced moisture
384 transport into the Iberian peninsula during the mid-Holocene led to more vegetation cover and increased
385 evapotranspiration and had a significant impact in reducing growing season temperatures. Differences in the
386 reconstructed trends of summer temperature and plant-available moisture through the Holocene suggests
387 that this land-surface feedback was not an important factor influencing summer temperatures in the
388 EMBSecBIO region. Nevertheless, differences in the strength of land-surface feedbacks between models could
389 also contribute to the divergences seen in the simulations. It would be useful to investigate the role of changes
390 in atmospheric circulation for precipitation patterns during the Holocene in the EMBSecBIO region using
391 transient simulations at higher resolution or regional climate models.

392 The timing of the transition to agriculture in the eastern Mediterranean is still debated (Asouti & Fuller, 2012).
393 It has been argued that climatic deterioration and population growth during the Younger Dryas triggered a
394 shift to farming (Weiss & Bradley, 2001; Bar-Yosef et al., 2017). The presence of morphologically altered
395 cereals by the end of the Pleistocene has been put forward as evidence for an early transition to agriculture
396 (Bar-Yosef et al., 2017), but it has also been pointed out that the evidence for cereal domestication before ca
397 10.5ka is poorly dated and insufficiently documented (Nesbitt, 2002) and that crops did not replace foraging
398 economies until well into the Holocene (Smith, 2001; Willcox, 2012; Zeder, 2011). The availability of water is
399 a crucial factor in the viability of early agriculture (Richerson et al., 2001; Zeder, 2011). We have shown that
400 moisture availability was higher than today during the first part of the Holocene (10-6 ka) but similar to today
401 until ca 10.5 ka. Wetter conditions during the early Holocene could have been a crucial factor in the transition
402 to agriculture, and our findings support the idea that this transition did not happen until much later than the

403 Younger Dryas or late glacial/Holocene transition. Further exploration of the role of climate in the transition
404 to agriculture would require a more comprehensive assessment of the archaeobotanical evidence. The issue
405 could also be addressed using modelling to explore how the reconstructed changes in regional moisture
406 availability and seasonal temperatures would impact crop viability (see e.g. Contreras et al., 2019).

407 We have focused on the composite picture of regional changes across the EMBSecBIO region, in order to
408 investigate whether these changes could be explained as a consequence of known changes in forcing. The
409 data set also provides information on the trends in climate at individual sites. These data could be used to
410 address the question of whether population density or cultural changes reflect shifts in climate (e.g. Weninger
411 et al., 2006; Drake, 2012; Kaniewski et al., 2013; Cookson et al., 2019; Weiberg et al., 2019; Palmisano et al.,
412 2021). In addition, it would also be possible to use these data to explore the impact of climate changes on the
413 environment, including the natural resources available for people (Harrison et al., 2023).

414

415 **5. Conclusions**

416 We have reconstructed changes in seasonal temperature and in plant-available moisture from 12.3 ka to the
417 present from 71 sites from the EMBSecBIO domain to examine changes in the regional climate of the eastern
418 Mediterranean region. We show that there are regionally coherent trends in these variables. The large
419 increase in both summer and winter temperatures during the early Holocene considerably post-dates the
420 warming observed elsewhere at the end of the Younger Dryas, supporting the idea that the impact of the
421 Younger Dryas in the EMBSecBIO region was muted. Subsequent changes in winter temperature are
422 consistent with the expected response to insolation changes. The timing of peak summer warming occurred
423 later than expected as a consequence of insolation changes and likely, at least in part, reflects the influence
424 of the relict Laurentide and Fennoscandian ice sheets on the regional climate. There is a rapid increase in
425 plant-available moisture between 11 and 10 ka, which could have promoted the adoption of agriculture in the
426 region.

427

428 **Data availability.**

429 Code for the reconstructions of the climatic variables:
430 https://github.com/esmeraldacs/EMBSecBIO_Holocene_climate

431 **Author Contributions**

432 ECS, SPH, ICP designed the study; EM, SPH and ECS revised EMBSecBIO database including the construction
433 of new age models; PJB, HR and YZ provided climate model output; ECS performed the analyses; SPH and ECS
434 wrote the first draft of the paper; all authors contributed to the final version.

435 **Competing Interests**

436 The authors declare there are no competing interests.

437 **Acknowledgements.**

438 We thank members of the SPECIAL team in Reading and from the Leverhulme Centre for Wildfires,
439 Environment and Society for useful discussions about these analyses.

440 **Financial support.**

441 ECS and SPH acknowledge funding support from the ERC-funded project GC2.0 (Global Change 2.0: Unlocking
442 the past for a clearer future, grant number 694481) and from the Leverhulme Centre for Wildfires,
443 Environment and Society through the Leverhulme Trust, grant number RC-2018-023.

444

445 **References**

- 446 Aksu, A. E., and Hiscott, R. N.: Persistent Holocene outflow from the Black Sea to the eastern Mediterranean
447 Sea still contradicts the Noah's Flood Hypothesis: A review of 1997–2021 evidence and a regional
448 paleoceanographic synthesis for the latest Pleistocene–Holocene, *Earth Sci. Rev.*, 227, 103960.
449 <https://doi.org/10.1016/j.earscirev.2022.103960>, 2022.
- 450 Bar-Matthews, M., Ayalon, A., and Kaufman, A.: Late Quaternary paleoclimate in the eastern Mediterranean
451 region from stable isotope analysis of speleothems at Soreq Cave, Israel, *Quat. Res.*, 47, 155-168,
452 <https://doi.org/10.1006/qres.1997.1883>, 1997.
- 453 Bartlein, P. J., Harrison, S.P., Brewer, S., Connor, S., Davis B.A.S., Gajewski, K., Guiot, J., Harrison-Prentice, T.
454 I., Henderson, A., Peyron, O., Prentice, I. C., Scholze, M., Seppä, H., Shuman, B., Sugita, S., Thompson, R. S.,
455 Viau, A., Williams, J., and Wu, H.: Pollen-based continental climate reconstructions at 6 and 21 ka: a global
456 synthesis, *Clim. Dynam.*, 37, 775–802, 2011.
- 457 Bartlein, P.J., Harrison, S.P., and Izumi, K.: Underlying causes of Eurasian mid-continental aridity in
458 simulations of mid-Holocene climate, *Geophys. Res. Lett.*, 44, 9020-9028, doi: 10.1002/2017GL074476, 2017.
- 459 Belfer-Cohen, A., & Goring-Morris, A. N. Becoming Farmers: The Inside Story. *Current Anthropology*, 52(S4),
460 S209–S220. <https://doi.org/10.1086/658861>, 2011.
- 461 Bereiter, B., Eggleston, S., Schmitt, J., Nehrbass-Ahles, C., Stocker, T.F., Fischer, H., Kipfstuhl, S., and
462 Chappellaz, J.: Revision of the EPICA Dome C CO₂ record from 800 to 600 kyr before present, *Geophys. Res.*
463 *Lett.*, 42, 542–549, <https://doi.org/10.1002/2014GL061957>, 2015.
- 464 Bini, M., Zanchetta, G., Perşoiu, A., Cartier, R., Català, A., Cacho, I., Dean, J.R., Di Rita, F., Drysdale, R.N.,
465 Finnè, M., Isola, I., Jalali, B., Lirer, F., Magri, D., Masi, A., Marks, L., Mercuri, A.M., Peyron, O., Sadori, L., ...
466 and Brisset, E.: The 4.2 ka BP Event in the Mediterranean region: An overview, *Clim. Past*, 15, 555–577,
467 <https://doi.org/10.5194/cp-15-555-2019>, 2019.
- 468 Bird, D., Miranda, L., Vander Linden, M., Robinson, E., Bocinsky, R.K., Nicholson, C., Capriles, J.M., Finley, J.B.,
469 Gayo, E.M., Gil, A., d'Alpoim Guedes, J., Hoggarth, J.A., Kay, A., Loftus, E., Lombardo, U., Mackie, M.,
470 Palmisano, A., Solheim, S., Kelly, R.L., and Freeman, J.: P3k14c, a synthetic global database of archaeological
471 radiocarbon dates, *Sci. Data*, 9, 27, <https://doi.org/10.1038/s41597-022-01118-7>, 2022.
- 472 Blaauw, M., Christen, J.A., Aquino Lopez, M.A., Vazquez, J.E., Gonzalez V.O.M., Belding, T., Theiler, J., Gough,
473 B., and Karney, C.: *rbacon: Age-Depth Modelling using Bayesian Statistics (2.5.6)* [R]. [https://CRAN.R-](https://CRAN.R-project.org/package=rbacon)
474 [project.org/package=rbacon](https://CRAN.R-project.org/package=rbacon), 2021. (last accessed 17 April 2023)
- 475 Blaschek, M., and Renssen, H.: The Holocene thermal maximum in the Nordic Seas: the impact of Greenland
476 Ice Sheet melt and other forcings in a coupled atmosphere-sea-ice-ocean model, *Clim. Past*, 9, 1629-1643,
477 [10.5194/cp-9-1629-2013](https://doi.org/10.5194/cp-9-1629-2013), 2013.
- 478 Bottema, S.: The Younger Dryas in the eastern Mediterranean, *Quat. Sci. Rev.*, 14, 883-891,
479 [https://doi.org/10.1016/0277-3791\(95\)00069-0](https://doi.org/10.1016/0277-3791(95)00069-0), 1995.
- 480 Burstyn, Y., Martrat, B., Lopez, J. F., Iriarte, E., Jacobson, M.J., Lone, M.A., and Deininger, M.: Speleothems
481 from the Middle East: An example of water limited environments in the SISAL database. *Quaternary*, 2, 16.
482 <https://doi.org/10.3390/quat2020016>, 2019.
- 483 Carré, M., Braconnot, P., Elliot, M., d'Agostino, R., Schurer, A., Shi, X., Marti, O., Lohmann, G., Jungclaus, J.,
484 Cheddadi, R., Abdelkader di Carlo, I., Cardich, J., Ochoa, D., Salas Gismondi, R., Pérez, A., Romero, P.E., Turcq,

485 B., Corrège, T., and Harrison, S.P.: High-resolution marine data and transient simulations support orbital
486 forcing of ENSO amplitude since the mid-Holocene. *Quat. Sci. Rev.*, 268, 107125.
487 <https://doi.org/10.1016/j.quascirev.2021.107125>, 2021.

488 Cheddadi, R., and Khater, C.: Climate change since the last glacial period in Lebanon and the persistence of
489 Mediterranean species, *Quat. Sci. Rev.*, 150, 146-157, <https://doi.org/10.1016/j.quascirev.2016.08.010>,
490 2016.

491 Cheng, H., Sinha, A., Verheyden, S., Nader, F.H., Li, X.L., Zhang, P.Z., Yin, J.J., Yi, L., Peng, Y.B., Rao, Z.G., Ning,
492 Y.F., and Edwards, R.L.: The climate variability in northern Levant over the past 20,000 years, *Geophys. Res.*
493 *Lett.*, 42, 8641–8650, <https://doi.org/10.1002/2015GL065397>, 2015.

494 Cheng, H., Zhang, H., Spötl, C., Baker, J., Sinha, A., Li, H., Bartolomé, M., Moreno, A., Kathayat, G., Zhao, J.,
495 Dong, X., Li, Y., Ning, Y., Jia, X., Zong, B., Ait Brahim, Y., Pérez-Mejías, C., Cai, Y., Novello, V.F., Cruz, F.W.,
496 Severinghaus, J.P., An, Z., and Edwards, R.L.: Timing and structure of the Younger Dryas event and its
497 underlying climate dynamics, *Proc. Natl. Acad. Sci. USA*, 117, 23408-23417, doi: 10.1073/pnas.2007869117,
498 2020.

499 Chevalier, M., Davis, B.A.S., Heiri, O., Seppä, H., Chase, B.M., Gajewski, K., Lacourse, T., Telford, R.J.,
500 Finsinger, W., Guiot, J., Kühl, N., Maezumi, S.Y., Tipton, J.R., Carter, V.A., Brussel, T., Phelps, L.N., Dawson, A.,
501 Zanon, M., Vallé, F., Nolan, C., Mauri, A., de Vernal, A., Izumi, K., Holmström, L., Marsicek, J., Goring, S.,
502 Sommer, P.S., Chaput, M., and Kupriyanov, D.: Pollen-based climate reconstruction techniques for late
503 Quaternary studies, *Earth Sci. Rev.*, 210, 103384, <https://doi.org/10.1016/j.earscirev.2020.103384>, 2020.

504 Cleveland, W.S., and Devlin, S.J.: Locally weighted regression: An approach to regression analysis by local
505 fitting, *J. Am. Stat. Assoc.*, 83, 596–610. <https://doi.org/10.1080/01621459.1988.10478639>, 1988.

506 Cookson, E., Hill, D.J., and Lawrence, D.: Impacts of long term climate change during the collapse of the
507 Akkadian Empire, *J. Arch. Sci.*, 106, 1-9, <https://doi.org/10.1016/j.jas.2019.03.009>, 2019.

508 Collins, W.D., Bitz, C.M., Blackmon, M.L., Bonan, G.B., Bretherton, C.S., Carton, J.A., Chang, P., Doney, S.C.,
509 Hack, J.J., Henderson, T.B., Kiehl, J.T., Large, W.G., McKenna, D.S., Santer, B.D., and Smith, R.D.: The
510 Community Climate System Model version 3 (CCSM3), *J. Clim.*, 19, 2122-2143,
511 <http://dx.doi.org/10.1175/JCLI3761.1>, 2006.
512

513 Connor, S., Colombaroli, D., Confortini, F., Gobet, E., Ilyashuk, B.P., Ilyashuk, E.A., van Leeuwen, J.F.N.,
514 Lamentowicz, M., van der Knaap, W.O., Malysheva, E., Marchetto, A., Margalitzadze, N., Mazei, Y., Mitchell,
515 E.A.D., Payne, R.J., and Ammann, B.: Long-term population dynamics: Theory and reality in a peatland
516 ecosystem, *J. Ecol.*, 106, 1, <https://doi.org/10.1111/1365-2745.12865>, 2017.

517 Contreras, D.A., Bondeau, A., Guiot, J., Kirman, A., Hiriart, E., Bernard, L., Suarez, R., Fader, M.: 2019. From
518 paleoclimate variables to prehistoric agriculture: Using a process-based agro-ecosystem model to simulate
519 the impacts of Holocene climate change on potential agricultural productivity in Provence, France, *Quat.*
520 *Internat.*, 501, 303-316

521 Cruz-Silva, E., Harrison, S.P., Marinova, E., and Prentice, I.C.: A new method based on surface-sample pollen
522 data for reconstructing palaeovegetation patterns, *J. Biogeog.*, 49, 1381–1396,
523 <https://doi.org/10.1111/jbi.14448>, 2022.

524 Dallmeyer, A., Claussen, M., Lorenz, S.J., and Shanahan, T.: The end of the African humid period as seen by a
525 transient comprehensive Earth system model simulation of the last 8000-years, *Clim. Past*, 16, 117–140,
526 <https://doi.org/10.5194/cp-16-117-2020>, 2020.

527 Davis, B.A.S., Brewer, S., Stevenson, A.C., and Guiot, J.: The temperature of Europe during the Holocene
528 reconstructed from pollen data, *Quat. Sci. Rev.*, 22: 1701-1716, [https://doi.org/10.1016/S0277-](https://doi.org/10.1016/S0277-3791(03)00173-2)
529 3791(03)00173-2, 2003.

530 Davis, T.W., Prentice, I.C., Stocker, B.D., Thomas, R.T., Whitley, R.J., Wang, H., Evans, B.J., Gallego-Sala, A.V.,
531 Sykes, M.T., and Cramer, W.: Simple process-led algorithms for simulating habitats (SPLASH v.1.0): Robust
532 indices of radiation, evapotranspiration and plant-available moisture, *Geosci. Model Dev.*, 10, 689–708,
533 <https://doi.org/10.5194/gmd-10-689-2017>, 2017.

534 Dean, J.R., Jones, M.D., Leng, M.J., Noble, S.R., Metcalfe, S.E., Sloane, H.J., Sahy, D., Eastwood, W.J., and
535 Roberts, C.N.: Eastern Mediterranean hydroclimate over the late glacial and Holocene, reconstructed from
536 the sediments of Nar lake, central Turkey, using stable isotopes and carbonate mineralogy, *Quat. Sci. Rev.*,
537 124, 162–174, <https://doi.org/10.1016/j.quascirev.2015.07.023>, 2015.

538 Denèfle, M., Lézine, A., Fouache, E., and Dufaure, J.: A 12,000-Year pollen record from Lake Maliq,
539 Albania, *Quat. Res.*, 54, 423-432, doi:10.1006/qres.2000.2179, 2000.

540 Drake, B.L.: The influence of climatic change on the Late Bronze Age Collapse and the Greek Dark Ages. *J.*
541 *Arch. Sci.*, 39, 1862–1870, <https://doi.org/10.1016/j.jas.2012.01.029>, 2012.

542 Flohr, P., Fleitmann, D., Matthews, R., Matthews, W., and Black, S.: Evidence of resilience to past climate
543 change in Southwest Asia: Early farming communities and the 9.2 and 8.2 ka events, *Quat. Sci. Rev.*, 136, 23–
544 39, <https://doi.org/10.1016/j.quascirev.2015.06.022>, 2016.

545 Goosse, H., Brovkin, V., Fichefet, T., Haarsma, R., Huybrechts, P., Jongma, J., Mouchet, A., Selten, F., Barriat,
546 P.-Y., Campin, J.-M., Deleersnijder, E., Driesschaert, E., Goelzer, H., Janssens, I., Loutre, M.-F., Morales
547 Maqueda, M. A., Opsteegh, T., Mathieu, P.-P., Munhoven, G., Pettersson, E. J., Renssen, H., Roche, D. M.,
548 Schaeffer, M., Tartinville, B., Timmermann, A., and Weber, S. L.: Description of the Earth system model of
549 intermediate complexity LOVECLIM version 1.2, *Geosci. Model Dev.*, 3, 603–633,
550 <https://doi.org/10.5194/gmd-3-603-2010>, 2010.

551 Goring-Morris, A.N., and Belfer-Cohen, A.: Evolving human/animal interactions in the Near Eastern Neolithic:
552 feasting as a case study, In G. Aranda, S. Monton, & M. Sanchez (Eds) *Guess Who's Coming to Dinner.*
553 *Feasting Rituals in the Prehistoric Societies of Europe and Near East*, pp. 64-72, Oxbow Books, Oxford, 2011.

554 Harrison, S.P.: Modern pollen data for climate reconstructions, version 1 (SMPDS) [Data set]. University of
555 Reading. <https://doi.org/10.17864/1947.194>, 2019. (last accessed 17 April 2023)

556 Harrison, S. P., and Prentice, I.C.: Climate and CO₂ controls on global vegetation distribution at the Last
557 Glacial Maximum: Analysis based on palaeovegetation data, biome modelling and palaeoclimate simulations,
558 *Glob. Change Biol.*, 9, 983–1004, <https://doi.org/10.1046/j.1365-2486.2003.00640.x>, 2003.

559 Harrison, S. P., Marinova, E., and Cruz-Silva, E.: EMBSecBIO pollen database [Data set]. University of Reading.
560 <https://doi.org/10.17864/1947.309>, 2021. (last accessed 17 April 2023)

561 Harrison, S.P., Prentice, I.C., Sutra J-P., Barboni, D., Kohfeld, K.E. and Ni. J.: Ecophysiological and bioclimatic
562 foundations for a global plant functional classification, *J. Veg. Sci.* 21, 300-317, doi:10.1111/j.1654-
563 1103.2009.01144x, 2010.

564 Harrison, S.P., Gaillard, M-J., Stocker, B., Vander Linden, M., Klein Goldewijk, K., Boles, O., Braconnot, P.,
565 Dawson, A., Fluet-Chouinard, E., Kaplan, J.O., Kastner, T., Pausata, F.S.R., Robinson, E., Whitehouse, N.,
566 Madella, M., Morrison, K.D.: Development and testing of scenarios for implementing Holocene LULC in Earth

567 System Model experiments, *Geosci. Model Dev.*, 13, 805-824, <https://doi.org/10.5194/gmd-13-805-2020>,
568 2020.

569 Harrison, S.P., Cruz-Silva, E., Haas, O., Liu, M., Parker, S., Qiao, S., Luke Sweeney, L., in press. Tools and
570 approaches to addressing the climate-humans nexus during the Holocene. *Proceedings of the 12th ICAANE*
571 *Congress*, Harrassowitz Verlag.

572 He, F., and Clark, P.U.: Freshwater forcing of the Atlantic Meridional Overturning Circulation revisited. *Nat.*
573 *Clim. Change*, 12, 449-454, <https://doi.org/10.1038/s41558-022-01328-2>, 2022.

574 Hengl, T.: Potential distribution of biomes (Potential Natural Vegetation) at 250 m spatial resolution [data
575 set], <https://doi.org/10.5281/zenodo.3526620>, 2019 (last accessed 17 April 2023)

576 Herzs Schuh, U., Böhmer, T., Li, C., Cao, X., Hébert, R., Dallmeyer, A., Telford, R.J. and Kruse, S.: Reversals in
577 temperature-precipitation correlations in the Northern Hemisphere extratropics during the
578 Holocene, *Geophys. Res. Lett.*, 49, e2022GL099730, <https://doi.org/10.1029/2022GL099730>, 2022.

579 Hill, M.O.: Diversity and evenness: A unifying notation and its consequences, *Ecol.* 54, 427–432,
580 <https://doi.org/10.2307/1934352>, 1973.

581 Jalut, G., Dedoubat, J.J., Fontugne, M., and Otto, T.: Holocene circum-Mediterranean vegetation changes:
582 Climate forcing and human impact, *Quat. Int.*, 200, 4–18, <https://doi.org/10.1016/j.quaint.2008.03.012>,
583 2009.

584 Joos, F., Gerber, S., Prentice, I.C., Otto-Bliesner, B.L., and Valdes, P.J.: Transient simulations of Holocene
585 atmospheric carbon dioxide and terrestrial carbon since the last glacial maximum, *Glob. Biogeochem. Cy.*,
586 18, GB2002, doi:10.1029/2003GB002156, 2004.

587 Kaniewski, D., Van Campo, E., Guiot, J., Le Burel, S., Otto, T., and Baeteman, C.: Environmental roots of the
588 Late Bronze Age Crisis. *PLoS ONE*, 8, e71004. <https://doi.org/10.1371/journal.pone.0071004>, 2013.

589 Kaplan, J.O., Krumhardt, K.M., Ellis, E.C., Ruddiman, W.F., Lemmen, C., and Klein Goldewijk, K.: Holocene
590 carbon emissions as a result of anthropogenic land cover change, *Holocene*, 21, 775-791, 2011.

591 Kapsch, M.-L., Mikolajewicz, U., Ziemen, F., and Schannwell, C.: Ocean response in transient simulations of
592 the last deglaciation dominated by underlying ice-sheet reconstruction and method of meltwater
593 distribution, *Geophys. Res. Lett.*, 49, e2021GL096767, <https://doi.org/10.1029/2021GL096767>, 2022.

594 Larsson, S.A., Kylander, M.E., Sannel, A.B.K., and Hammarlund, D.: Synchronous or not? The timing of the
595 Younger Dryas and Greenland Stadial-1 reviewed using tephrochronology. *Quaternary*, 5, 19,
596 <https://doi.org/10.3390/quat5020019>, 2022.

597 Liu, M., Prentice, I.C., ter Braak, C.J.F., and Harrison, S.P.: An improved statistical approach for reconstructing
598 past climates from biotic assemblages, *Proc. Roy. Soc. A: Math., Phys. Eng. Sci.*, 476, 20200346.
599 <https://doi.org/10.1098/rspa.2020.0346>, 2020.

600 Liu, M., Shen, Y., González-Sampéris, P., Gil-Romera, G., ter Braak, C.J.F. Prentice, I.C., and Harrison, S.P.:
601 Holocene climates of the Iberian Peninsula, *Clim. Past*, 19, 803-834, [https://doi.org/10.5194/cp-19-803-](https://doi.org/10.5194/cp-19-803-2023)
602 2023, 2023.

603 Liu, Z., Otto-Bliesner, B. L., He, F., Brady, E. C., Tomas, R., Clark, P. U., Carlson, A. E., Lynch-Stieglitz, J., Curry,
604 W., Brook, E., Erickson, D., Jacob, R., Kutzbach, J., and Cheng, J.: Transient Simulation of Last Deglaciation

605 with a New Mechanism for Bolling-Allerod Warming, *Science*, 325, 310-314,
606 doi:10.1126/science.1171041, 2009.

607

608 Magyari, E.K., Pál, I., Vincze, I., Veres, D., Jakab, G., Braun, M., Szalai, Z., Szabó, Z., and Korponai, J.: Warm
609 Younger Dryas summers and early late glacial spread of temperate deciduous trees in the Pannonian Basin
610 during the last glacial termination (20-9 kyr cal BP), *Quat. Sci. Rev.*, 225, 105980,
611 doi.org/10.1016/j.quascirev.2019.105980, 2019.

612 Marinova, E., Harrison, S.P., Bragg, F., Connor, S., de Laet, V., Leroy, S.A.G., Mudie, P., Atanassova, J.,
613 Bozilova, E., Caner, H., Cordova, C., Djamali, M., Filipova-Marinova, M., Gerasimenko, N., Jahns, S., Kouli, K.,
614 Kotthoff, U., Kvavadze, E., Lazarova, M., ... and Tonkov, S.: Pollen-derived biomes in the Eastern
615 Mediterranean–Black Sea–Caspian–Corridor, *J. Biogeog.*, 45, 484–499, <https://doi.org/10.1111/jbi.13128>,
616 2018.

617 Martin Calvo, M., and Prentice, I.C.: Effects of fire and CO₂ on biogeography and primary production in glacial
618 and modern climates, *New Phytol.*, 208, 987–994. <https://doi.org/10.1111/nph.13485>, 2015.

619 Mauri, A., Davis, B.A.S., Collins, P.M., and Kaplan, J.O.: The influence of atmospheric circulation on the mid-
620 Holocene climate of Europe: a data–model comparison, *Clim. Past*, 10, 1925–1938,
621 <https://doi.org/10.5194/cp-10-1925-2014>, 2014.

622 Mauri, A., Davis, B.A.S., Collins, P.M., Kaplan, J.O.: The climate of Europe during the Holocene: a gridded
623 pollen-based reconstruction and its multi-proxy evaluation, *Quat. Sci. Rev.*, 112, 109-127,
624 <https://doi.org/10.1016/j.quascirev.2015.01.013>, 2015.

625 Messenger, E., Belmecheri, S., Von Grafenstein, U., Vincent, O., Voinchet, P., Puaud, S., Courtin-nomade, A.,
626 Guillou, H., Mgeladze, A., Dumoulin, J.-P., Mazuy, A., and Lordkipanidze, D.: Late Quaternary record of the
627 vegetation and catchment-related changes from Lake Paravani (Javakheti, South Caucasus), *Quat. Sci. Rev.*,
628 77, 125–140, <https://doi.org/10.1016/j.quascirev.2013.07.011>, 2013.

629 Mitchell, L., Brook, E., Lee, J., Buizert, C., and Sowers, T.: Constraints on the late Holocene anthropogenic
630 contribution to the atmospheric methane budget, *Science*, 342, 964–966, doi:10.1126/science.1238920,
631 2013.

632 New, M., Lister, D., Hulme, M., and Makin, I.: A high-resolution data set of surface climate over global land
633 areas, *Clim. Res.*, 21, 1–25. <https://doi.org/10.3354/cr021001>, 2002.

634 Otto-Bliesner, B.L., Braconnot, P., Harrison, S.P., Lunt, D.J., Abe-Ouchi, A., Albani, S., Bartlein, P.J., Capron, E.,
635 Carlson, A.E., Dutton, A., Fischer, H., Goelzer, H., Govin, A., Haywood, A., Joos, F., LeGrande, A.N., Lipscomb,
636 W.H., Lohmann, G., Mahowald, N., ... and Zhang, Q.: The PMIP4 contribution to CMIP6 – Part 2: Two
637 interglacials, scientific objective and experimental design for Holocene and Last Interglacial simulations,
638 *Geosci. Model Dev.*, 10, 3979–4003. <https://doi.org/10.5194/gmd-10-3979-2017>, 2017.

639 Palmisano, A., Bevan, A., Kabelindde, A., Roberts, N., and Shennan, S.: Long-term demographic trends in
640 prehistoric Italy: Climate impacts and regionalised socio-ecological trajectories, *J. World Prehist.*, 34, 381–
641 432, <https://doi.org/10.1007/s10963-021-09159-3>, 2021.

642 Patton, H., Hubbard, A., Andreassen, K., Auriac, A., Whitehouse, P.L., Stroeven, A.P., Shackleton, C.,
643 Winsborrow, M., Heyman, J., and Hall, A.M.: Deglaciation of the Eurasian ice sheet complex, *Quat. Sci. Rev.*,
644 169, 148–172, <https://doi.org/10.1016/j.quascirev.2017.05.019>, 2017.

645 Prentice, I.C., Harrison, S.P., and Bartlein, P.J.: Global vegetation and terrestrial carbon cycle changes after
646 the last ice age, *New Phytol.* 189, 988–998, <https://doi.org/10.1111/j.1469-8137.2010.03620.x>, 2011.

647 Prentice, I.C., Villegas-Diaz, R., and Harrison, S.P.: Accounting for atmospheric carbon dioxide variations in
648 pollen-based reconstruction of past hydroclimates, *Glob. Planet. Change*, 211, 103790.
649 <https://doi.org/10.1016/j.gloplacha.2022.103790>, 2022.

650 Prentice, I.C., Villegas-Diaz, R., and Harrison, S.P.: *codos: 0.0.2* (0.0.2). Zenodo.
651 <https://doi.org/10.5281/ZENODO.5083309>, 2022 (last accessed 17 April 2023)

652 Reimer, P., Austin, W. E. N., Bard, E., Bayliss, A., Blackwell, P. G., Ramsey, C. B., Butzin, M., Cheng, H.,
653 Edwards, R. L., Friedrich, M., Grootes, P. M., Guilderson, T. P., Hajdas, I., Heaton, T. J., Hogg, A. G., Hughen, K.
654 A., Kromer, B., Manning, S. W., Muscheler, R., ... and Talamo, S.: The IntCal20 Northern Hemisphere
655 radiocarbon age calibration curve (0-55 cal kBP), *Radiocarbon*, 62, 725-757,
656 <https://doi.org/10.1017/RDC.2020.41>, 2020.

657 Renssen, H., Seppä, H., Heiri, O., Roche, D.M., Goosse, H., and Fichet, T.: The spatial and temporal
658 complexity of the Holocene thermal maximum, *Nat. Geosci.* 2, 411–414, <https://doi.org/10.1038/ngeo513>,
659 2009.

660 Richerson, P.J., Boyd, R., and Bettinger, R.L.: Was agriculture impossible during the Pleistocene but
661 mandatory during the Holocene? A climate change hypothesis, *Am. Antiq.*, 66, 387–411,
662 <https://doi.org/10.2307/2694241>, 2001.

663 Roberts, N., Brayshaw, D., Kuzucuoğlu, C., Perez, R., and Sadori, L.: The mid-Holocene climatic transition in
664 the Mediterranean: Causes and consequences, *Holocene*, 21, 3–13,
665 <https://doi.org/10.1177/0959683610388058>, 2011.

666 Roberts, N., Cassis, M., Doonan, O., Eastwood, W., Elton, H., Haldon, J., Izdebski, A., and Newhard, J.: Not the
667 End of the World? Post-classical decline and recovery in rural Anatolia, *Hum. Ecol.*, 46, 305–322,
668 <https://doi.org/10.1007/s10745-018-9973-2>, 2018.

669 Roberts, C.N., Woodbridge, J., Palmisano, A., Bevan, A., Fyfe, R., and Shennan, S.: Mediterranean landscape
670 change during the Holocene: Synthesis, comparison and regional trends in population, land cover and
671 climate, *Holocene*, 29, 923–937, <https://doi.org/10.1177/0959683619826697>, 2019.

672 Roffet-Salque, M., Marciniak, A., Valdes, P.J., Pawłowska, K., Pyzel, J., Czerniak, L., Krüger, M., Roberts, C.N.,
673 Pitter, S., Evershed, R.P.: Evidence for the impact of the 8.2-ky BP climate event on Near Eastern early
674 farmers, *Proc Natl Acad Sci USA*, 115, 8705-8709, doi: 10.1073/pnas.1803607115. 2018.

675 Ruddiman, W. F.: The anthropogenic greenhouse era began thousands of years ago, *Clim. Change*, 61, 261–
676 293, doi:10.1023/B:CLIM.0000004577.17928.fa, 2003.

677 Rymes, M.D., and Myers, D.R.: Mean preserving algorithm for smoothly interpolating averaged data. *Solar*
678 *Energy*, 71, 225–231, [https://doi.org/10.1016/S0038-092X\(01\)00052-4](https://doi.org/10.1016/S0038-092X(01)00052-4), 2001.

679 Sadori, L., Jahns, S., and Peyron, O.: Mid-Holocene vegetation history of the central Mediterranean,
680 *Holocene*, 21, 117-129, <https://doi.org/10.1177/0959683610377530>, 2011.

681 Sidorenko, D., Goessling, H. f., von Koldunov, N., Scholz, P., Danilov, S., Barbi, D., Cabos, W., Gurses, O.,
682 Harig, S., Hinrichs, C., Juricke, S., Lohmann, G., Losch, M., Mu, L., Rackow, T., Rakowsky, N., Sein, D.,
683 Semmler, T., Shi, X., ... and Jung, T.: Evaluation of FESOM2.0 coupled to ECHAM6.3: Preindustrial and

684 HighResMIP simulations, *J. Adv. Model. Earth Syst.*, 11, 3794–3815, <https://doi.org/10.1029/2019MS001696>,
685 2019.

686 Singarayer, J.S., Valdes, P.J., Friedlingstein, P., Nelson, S., and Beerling, D.J.: Late Holocene methane rise
687 caused by orbitally controlled increase in tropical sources, *Nature*, 470, 82–85, doi:10.1038/nature09739,
688 2011.

689 Stocker, B.D., Yu, Z., Massa, C., and Joos, F.: Holocene peatland and ice-core data constraints on the timing
690 and magnitude of CO₂ emissions from past land use, *Proc. Natl. Acad. Sci.*, 114, 1492–1497,
691 doi:10.1073/pnas.1613889114, 2017.

692 Vadsaria, T., Zaragosi, S., Ramstein, G., Dutay, J.-C., Li, L., Siani, G., Revel, M., Obase, T., and Abe-Ouchi,
693 A.: Freshwater influx to the Eastern Mediterranean Sea from the melting of the Fennoscandian ice sheet
694 during the last deglaciation, *Sci. Rep.* 12, 8466, <https://doi.org/10.1038/s41598-022-12055-1>, 2022.

695 Villegas-Diaz, R., and Harrison, S. P.: The SPECIAL Modern Pollen Data Set for Climate Reconstructions,
696 version 2 (SMPDSv2), University of Reading. Dataset, <https://doi.org/10.17864/1947.000389>, 2022. (last
697 accessed 17 April 2023).

698 Villegas-Diaz, R., and Harrison, S.P.: *smpds*: The SPECIAL Modern Pollen Data Set for Climate Reconstructions
699 (v2.0.0). Zenodo. <https://doi.org/10.5281/ZENODO.6598832>, 2022. (last accessed 17 April 2023)

700 Villegas-Diaz, R., Cruz-Silva, E., and Harrison, S.P.: *ageR*: Supervised Age Models [R]. Zenodo.
701 <https://doi.org/10.5281/zenodo.4636716>, 2021 (last accessed 17 April 2023).

702 Villegas-Diaz, R., Prentice, I.C., and Harrison, S.P.: *COdos*: CO₂ Correction Tools [R]. SPECIAL Research Group.
703 <https://github.com/special-uor/codos>, 2022. (last accessed 17 April 2023)

704 Wei, D., González-Sampériz, P., Gil-Romera, G., Harrison, S.P., and Prentice, I.C.: Seasonal temperature and
705 moisture changes in interior semi-arid Spain from the last interglacial to the Late Holocene, *Quat. Res.*, 101,
706 143–155. <https://doi.org/10.1017/qua.2020.108>, 2021.

707 Weiberg, E., Bevan, A., Kouli, K., Katsianis, M., Woodbridge, J., Bonnier, A., Engel, M., Finné, M., Fyfe, R.,
708 Maniatis, Y., Palmisano, A., Panajiotidis, S., Roberts, C. N., and Shennan, S.: Long-term trends of land use and
709 demography in Greece: A comparative study, *Holocene*, 29, 742–760,
710 <https://doi.org/10.1177/0959683619826641>, 2019.

711 Weninger, B., Alram-Stern, E., Bauer, E., Clare, L., Danzeglocke, U., Jöris, O., Kubatzki, C., Rollefson, G.,
712 Todorova, H., and van Andel, T.: Climate forcing due to the 8200 cal yr BP event observed at Early Neolithic
713 sites in the eastern Mediterranean, *Quat. Res.*, 66, 401–420, <https://doi.org/10.1016/j.yqres.2006.06.009>,
714 2006.

715

716 Yanchilina, A.G., Ryan, W.B.F., Kenna, T.C., and McManus, J.F.: Meltwater floods into the Black and Caspian
717 Seas during Heinrich Stadial 1, *Earth Sci. Rev.*, 198, 102931, <https://doi.org/10.1016/j.earscirev.2019.102931>,
718 2019.

719

720 Zeder, M.A.: The origins of agriculture in the Near East, *Curr. Anthropol.*, 52), S221–S235,
721 <https://doi.org/10.1086/659307>, 2011.

722 Zhang, Y., Renssen, H., and Seppä, H.: Effects of melting ice sheets and orbital forcing on the early Holocene
723 warming in the extratropical Northern Hemisphere, *Clim. Past*, 12, 1119–1135. <https://doi.org/10.5194/cp-12-1119-2016>, 2016.

724

725 Zhang, Y., Renssen, H., Seppä, H., and Valdes, P. J.: Holocene temperature trends in the extratropical
726 Northern Hemisphere based on inter-model comparisons, *J. Quat. Sci.*, 33, 464–476.
727 <https://doi.org/10.1002/jqs.3027>, 2018.

728 **Figure and Table Captions**

729 Figure 1. Distribution of pollen records used in the climate reconstructions. The colour coding shows the length
730 of the record.

731 Figure 2. Time series of reconstructed anomalies of mean temperature of the coldest month (MTCO) for
732 individual records. Entities are arranged by latitude (N-S). Information about the numbered individual sites
733 can be found in Supplementary Table 1.

734 Figure 3. Time series of reconstructed anomalies of mean temperature of the warmest month (MTWA) for
735 individual records. Entities are arranged by latitude (N-S). Information about the numbered individual sites
736 can be found in Supplementary Table 1.

737 Figure 4. Time series of reconstructed anomalies of plant available moisture, expressed as the ratio between
738 potential and actual evapotranspiration (α), at individual sites. A correction to account for the direct
739 physiological impacts of CO₂ on plant growth has been applied to the reconstructed α . Entities are arranged
740 by latitude (N-S). Information about the numbered individual sites can be found in Supplementary Table 1.

741 Figure 5. Composite changes in reconstructed mean temperature of the coldest month (MTCO), mean
742 temperature of the warmest month (MTWA), growing degree days above a base level of 0°C (GDD0), and plant
743 available moisture expressed as the ratio between potential and actual evapotranspiration (α). A correction
744 to account for the direct physiological impacts of CO₂ on plant growth has been applied to the reconstructions
745 of α . The dark blue line is a loess smoothed curve through the reconstruction with a window half width of 500
746 years; the green shading shows the uncertainties based on 1000 bootstrap resampling of the records. The
747 bottom panel shows the number of records used to create the composite through time.

748 Figure 6. Simulated regional changes in mean temperature of the coldest month (MTCO), mean temperature
749 of the warmest month (MTWA), growing degree days above a base level of 0°C (GDD0), and plant available
750 moisture expressed as the ratio between potential and actual evapotranspiration (α) in the EMBSecBIO
751 domain from the TRACE-21K-I (green) and TRACE-21K-II (red) transient simulations. It is not possible to
752 calculate changes in α for the TRACE-21K-II simulation from the available data. Loess smoothed curves were
753 drawn using a window half width of 500 years, and the envelope was obtained through 1000 bootstrap
754 resampling of the sequences. The top panel shows the changes in summer and winter insolation (Wm^{-2}) at 40°
755 N.

756 Figure 7. Simulated regional changes in mean temperature of the coldest month (MTCO), mean temperature
757 of the warmest month (MTWA), and growing degree days above a base level of 0°C (GDD0) in the EMBSecBIO
758 domain from the LOVECLIM transient simulation. It is not possible to calculate changes in α for the LOVECLIM
759 simulation from the available data. Loess smoothed curves were drawn using a window half width of 500
760 years, and the envelope was obtained through 1000 bootstrap resampling of the sequences.

761 Figure 8. Simulated regional changes in mean temperature of the coldest month (MTCO), mean temperature
762 of the warmest month (MTWA), and growing degree days above a base level of 0°C (GDD0) in the EMBSecBIO
763 domain from the four PACMEDY simulations. The models are: Max Plank Institute Earth System Model (MPI),
764 Alfred Wagener Institute Earth System Model simulations (AWI), Institute Pierre Simon Laplace Climate Model

765 TR5AS simulation (IPSL-CM5) and Institute Pierre Simon Laplace Climate Model TR6A V simulation (IPSL-CM6).
766 Loess smoothed curves were drawn using a window half width of 500 years and the envelope was obtained
767 through 1000 bootstrap resampling of the sequences.

768 Figure 9. Comparison of regional composites of reconstructed seasonal temperatures from this study with
769 those derived from Mauri et al. (2015) and Herzschuh et al. (2022). Mauri et al. (2015 provide mean
770 temperature of the coldest month (MTCO) and mean temperature of the warmest month (MTWA)
771 reconstructions, which can be directly compared with our reconstructions. Herzschuh et al. (2022) only
772 provide reconstructions of July temperature. Our reconstructions are shown in blue, reconstructions based on
773 the Mauri et al. (2015) data set are shown in green, and reconstructions based on the Herzschuh et al.
774 reconstruction are shown in orange. The solid line is a loess smoothed curve through the reconstruction with
775 a window half width of 500 years; the shading shows the uncertainties based on 1000 bootstrap resampling
776 of the records.

777 Table 1. Leave-out cross-validation fitness of fxTWA-PLSv2 for mean temperature of the coldest month
778 (MTCO), mean temperature of the warmest month (MTWA), growing degree days above base level 0°C (GDD0)
779 and plant-available moisture (α) with p-spline smoothed fx estimation, using bins of 0.02, 0.02 and 0.002,
780 showing results for the selected component for each variable. RMSEP is the root-mean-square error of
781 prediction. p assesses whether using the current number of components is significantly different from using
782 one component less. The degree of overall compression is assessed by linear regression of the cross-validated
783 reconstructions onto the climate variable, where b1 and b1.se are the slope and the standard error of the
784 slope, respectively. The overall compression is reduced as the slope approaches 1. Full details for all the
785 components are given in Supplementary Table 4.

786

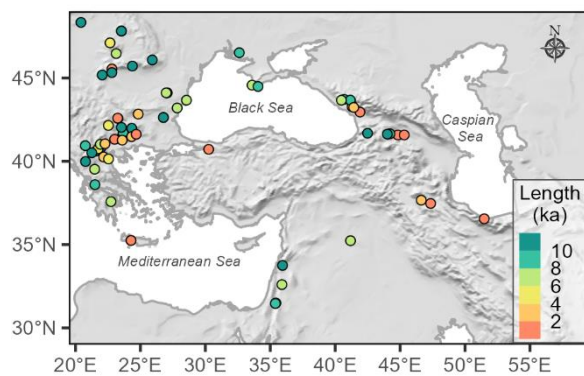
787

788

789

790

791 Figure 1. Distribution of pollen records used in the climate reconstructions. The colour coding shows the
792 length of the record.



793

794

795

796

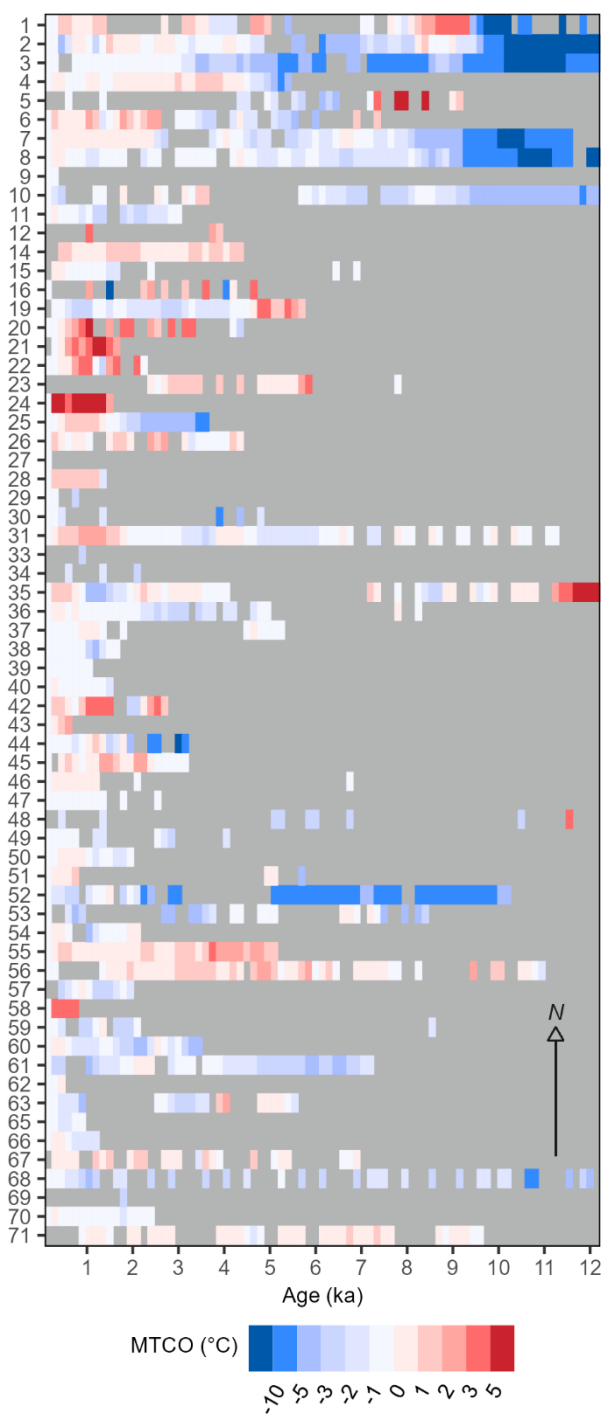
797

798

799

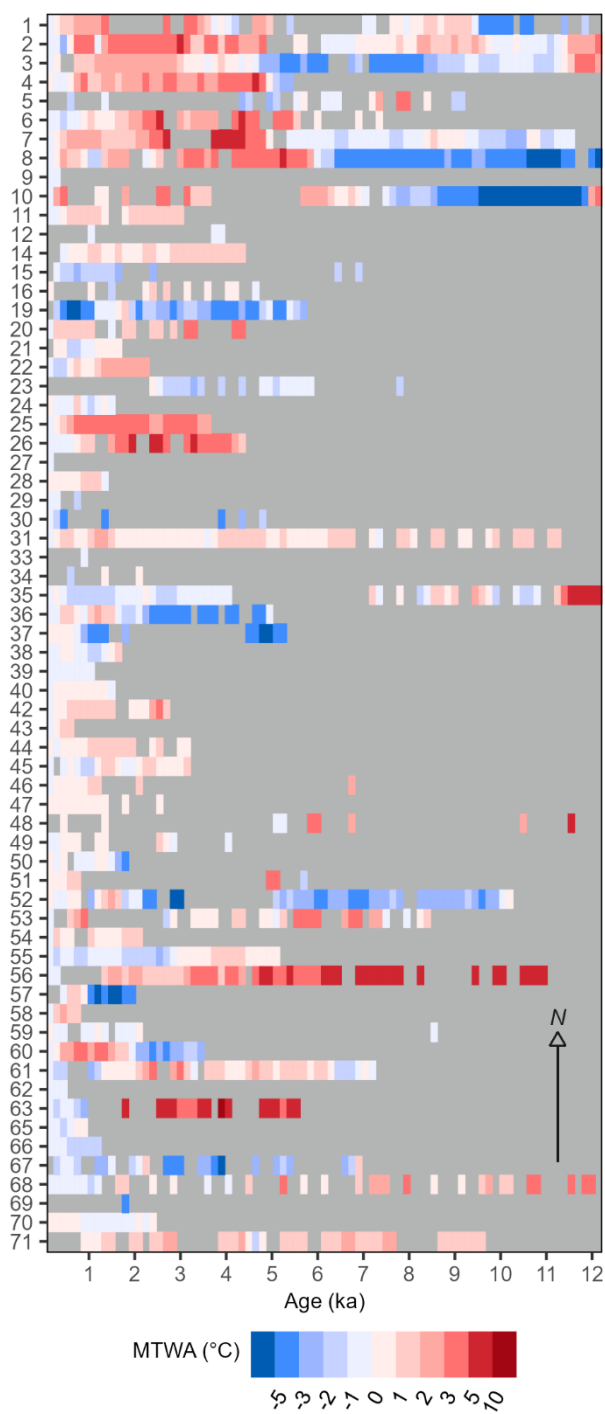
800

801 Figure 2. Time series of reconstructed anomalies of mean temperature of the coldest month (MTCO) for
802 individual records. Entities are arranged by latitude (N-S). Information about the numbered individual sites
803 can be found in Supplementary Table 1.



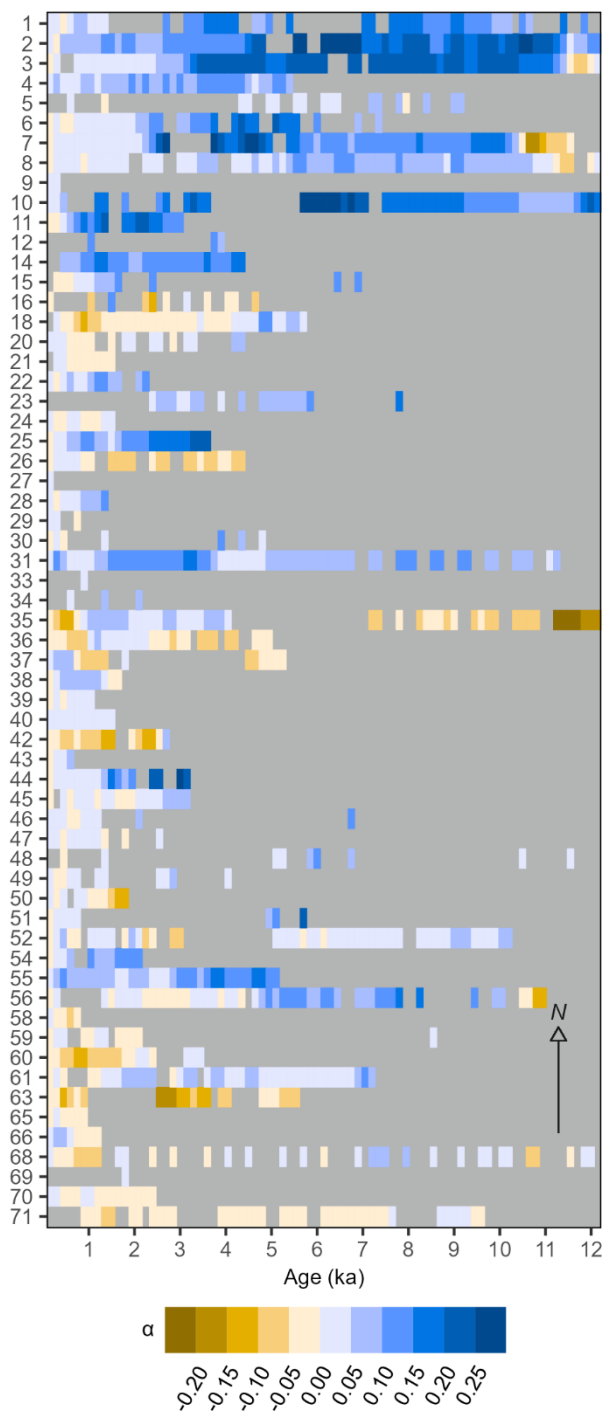
804
805
806
807
808

809 Figure 3. Time series of reconstructed anomalies of mean temperature of the warmest month (MTWA) for
810 individual records. Entities are arranged by latitude (N-S). Information about the numbered individual sites
811 can be found in Supplementary Table 1.



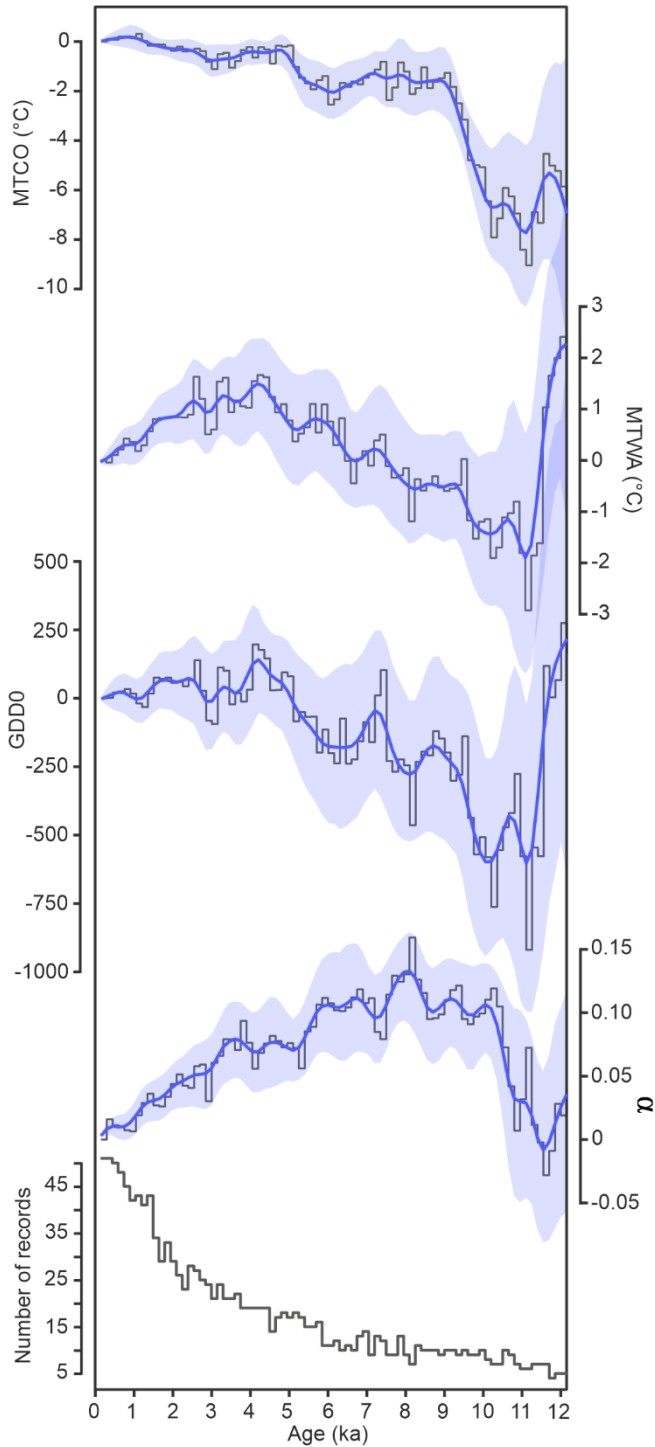
812
813
814
815

816 Figure 4. Time series of reconstructed anomalies of plant available moisture, expressed as the ratio between
817 potential and actual evapotranspiration (α), at individual sites. A correction to account for the direct
818 physiological impacts of CO₂ on plant growth has been applied to the reconstructed α . Entities are arranged
819 by latitude (N-S).



820
821
822

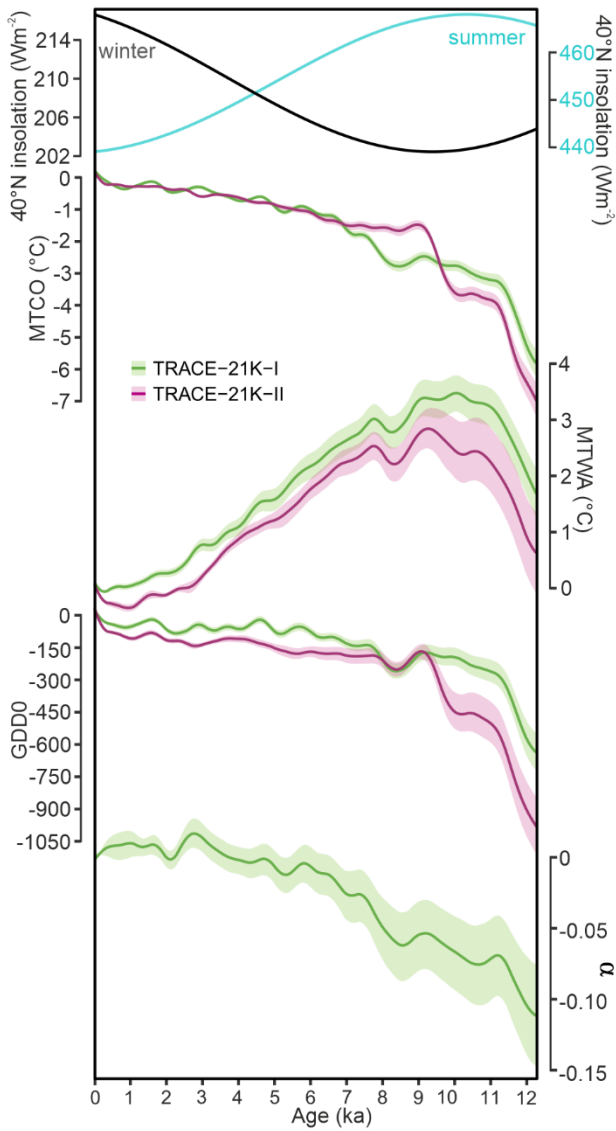
823 Figure 5. Composite changes in reconstructed mean temperature of the coldest month (MTCO), mean
 824 mean temperature of the warmest month (MTWA), growing degree days above a base level of 0°C (GDD0), and
 825 plant available moisture expressed as the ratio between potential and actual evapotranspiration (α). A
 826 correction to account for the direct physiological impacts of CO₂ on plant growth has been applied to the
 827 reconstructions of α . The dark blue line is a loess smoothed curve through the reconstruction with a window
 828 half width of 500 years; the blue shading shows the uncertainties based on 1000 bootstrap resampling of the
 829 records. The bottom panel shows the number of records used to create the composite through time.



830

831

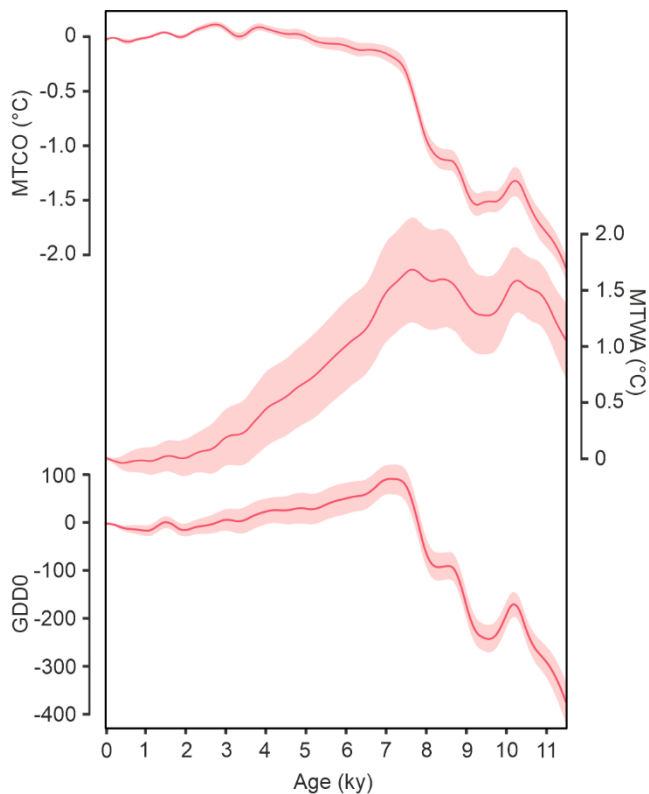
832 Figure 6. Simulated regional changes in mean temperature of the coldest month (MTCO), mean temperature
 833 of the warmest month (MTWA), growing degree days above a base level of 0°C (GDD0), and plant available
 834 moisture expressed as the ratio between potential and actual evapotranspiration (α) in the EMBSecBIO
 835 domain from the TRACE-21K-I (green) and TRACE-21K-II (red) transient simulations. It is not possible to
 836 calculate changes in α for the TRACE-21K-II simulation from the available data. Loess smoothed curves were
 837 drawn using a window half width of 500 years, and the envelope was obtained through 1000 bootstrap
 838 resampling of the sequences. The top panel shows the changes in summer and winter insolation (Wm^{-2}) at 40°
 839 N.



840
 841
 842
 843
 844
 845
 846

847

848 Figure 7. Simulated regional changes in mean temperature of the coldest month (MTCO), mean temperature
849 of the warmest month (MTWA), and growing degree days above a base level of 0°C (GDD0) in the EMBSeCBIO
850 domain from the LOVECLIM transient simulation. It is not possible to calculate changes in α for the LOVECLIM
851 simulation from the available data. Loess smoothed curves were drawn using a window half width of 500
852 years, and the envelope was obtained through 1000 bootstrap resamplings of the sequences.



853

854

855

856

857

858

859

860

861

862

863

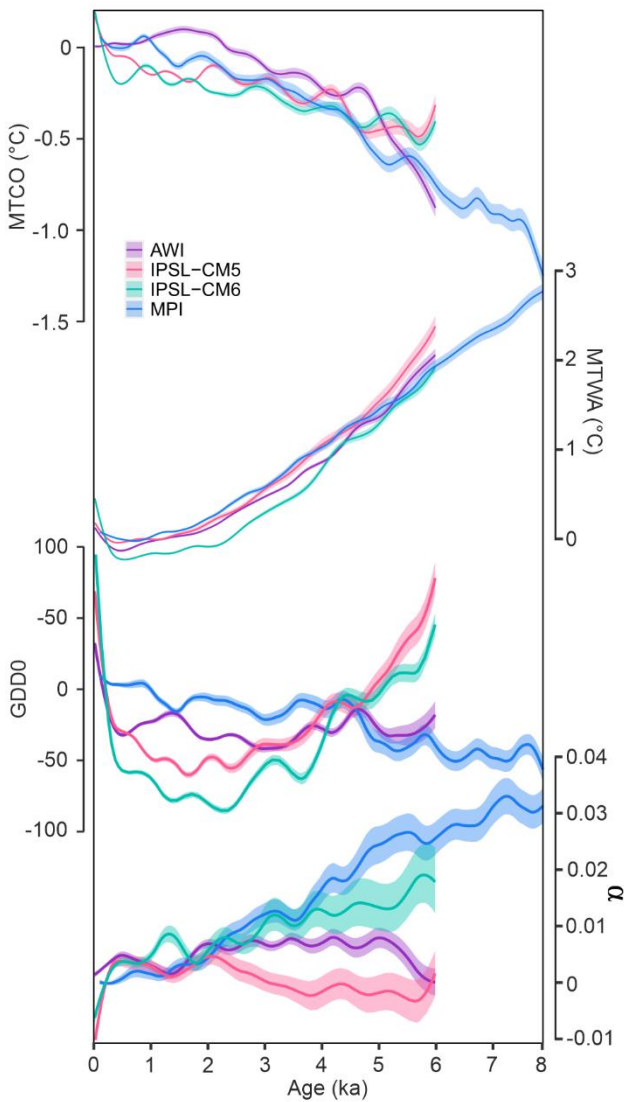
864

865

866

867

868 Figure 8. Simulated regional changes in mean temperature of the coldest month (MTCO), mean temperature
869 of the warmest month (MTWA), and growing degree days above a base level of 0°C (GDD0) in the
870 EMBSecBIO domain from the four PACMEDY simulations. The models are: Max Plank Institute Earth System
871 Model (MPI), Alfred Wagener Institute Earth System Model simulations (AWI), Institute Pierre Simon Laplace
872 Climate Model TR5AS simulation (IPSL-CM5) and Institute Pierre Simon Laplace Climate Model TR6A V
873 simulation (IPSL-CM6). Loess smoothed curves were drawn using a window half width of 500 years and the
874 envelope was obtained through 1000 bootstrap resampling of the sequences.



875

876

877

878

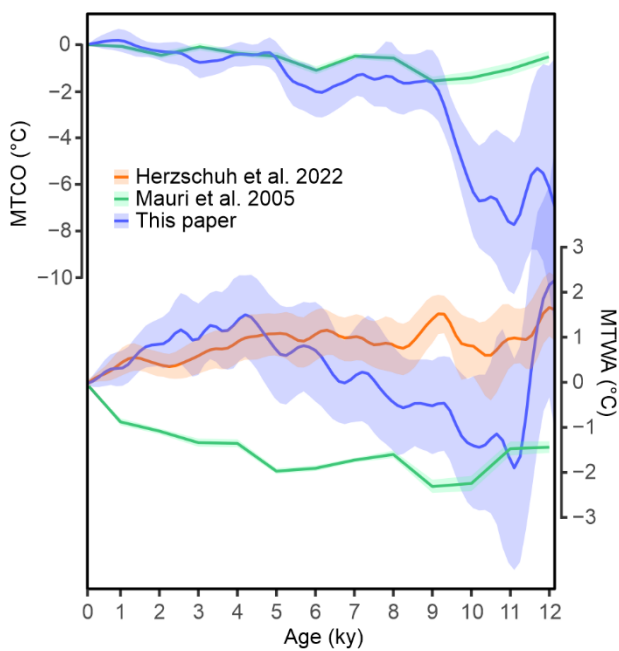
879

880

881

882

883 Figure 9. Comparison of regional composites of reconstructed seasonal temperatures from this study with
884 those derived from Mauri et al. (2015) and Herzschuh et al. (2022). Mauri et al. (2015 provide mean
885 temperature of the coldest month (MTCO) and mean temperature of the warmest month (MTWA)
886 reconstructions, which can be directly compared with our reconstructions. Herzschuh et al. (2022) only
887 provide reconstructions of July temperature. Our reconstructions are shown in blue, reconstructions based on
888 the Mauri et al. (2015) data set are shown in green, and reconstructions based on the Herzschuh et al.
889 reconstruction are shown in orange. The solid line is a loess smoothed curve through the reconstruction with
890 a window half width of 500 years; the shading shows the uncertainties based on 1000 bootstrap resampling
891 of the records.



892

893

894

895 **Table 1.** Leave-out cross-validation fitness of fxTWA-PLSv2 for mean temperature of the coldest month
 896 (MTCO), mean temperature of the warmest month (MTWA), growing degree days above base level 0°C (GDD0)
 897 and plant-available moisture (α) with p-spline smoothed fx estimation, using bins of 0.02, 0.02 and 0.002,
 898 showing results for the selected component for each variable. RMSEP is the root-mean-square error of
 899 prediction. p assesses whether using the current number of components is significantly different from using
 900 one component less. The degree of overall compression is assessed by linear regression of the cross-validated
 901 reconstructions onto the climate variable, where b1 and b1.se are the slope and the standard error of the
 902 slope, respectively. The overall compression is reduced as the slope approaches 1. Full details for all the
 903 components are given in Supplementary Table 4.

Variable	Selected component	R2	Average bias	RMSEP	p	b1	b1.se
MTCO	4	0.73	-0.22	3.67	0.001	0.86	0.01
MTWA	2	0.63	-0.10	3.22	0.001	0.78	0.01
GDD0	2	0.69	56.46	880.33	0.001	0.79	0.01
α	2	0.73	-0.01	0.15	0.001	0.80	0.01

904

905

906

907

908

909

910

911

912

913

914